MET.O.14

METEOROLOGICAL OFFICE
BOUNDARY LAYER RESEARCH BRANCH
TURBULENCE & DIFFUSION NOTE

T.D.N. No. 160

A numerical study of cloud streets in the planetary boundary layer.

by

Dr. P.J. Mason

Meteorological Research Unit
R.A.F. Cardington
Bedford.

OCT 1984.

Summary

A two-dimensional numerical model is used to study the influence of small non-precipitating clouds on horizontal roll vortices in the planetary boundary layer. The model explicitly represents the large scale two-dimensional motions whilst small scale eddies are parametrized by a buoyancy dependent mixing length hypothesis. It is applied to conditions corresponding to an observed case of cloud street formation.

Introduction

The appearance of cloud streets in the planetary boundary layer has attracted much interest. These streets usually arise in moderate or strong winds in conditions with a significant upward heat flux (Le Mone 1973) and have been shown to be associated with large scale longitudinal roll motions in the planetary boundary layer. They have also been detected in clear air (Reinking et al. 1981) and the presence of clouds is regarded as a consequence rather than a cause of the roll motions.

The cause of the roll motions has been attributed to both a shear instability of the planetary Ekman boundary layer and to the organisation of buoyant convection by velocity shear. Both observations and detailed studies show the latter dynamics to be the most usual mechanism. The present work extends the previous studies of such buoyancy driven motion by Mason and Sykes 1982 (referred to hereafter as M & S) and Mason 1983, to include the effects of water vapour and non-precipitating clouds with cloud top cooling. It provides a detailed and quantitative appraisal of the influence of these factors upon the roll motions. However since the model being used only supports large scale two-dimensional motions it cannot predict whether two-dimensional rolls should actually dominate the flow. It can only serve to clarify the properties of any two-dimensional structures which may exist. For this reason the model has been applied to conditions under which marked cloud streets have been observed. The conditions occurred over the North Sea during the KONTUR experiment (Hoeber 1982).

In both the observations and the results the clouds formed are typical of fair weather cumulus. The boundary layer over the sea is characterised by a low value of surface stress and surface heat flux and these clouds assume more dynamical importance than would be usual over land. In common with other observations of fairly steady boundary layers with broken cloud cover, the air above the boundary layer is of low relative humidity. This gives rise to cloud top entrainment instability (Randall 1980a, Deardorff 1980a) which promotes boundary layer entrainment of dry air and inhibits the formation of more solid cloud cover. The respective roles of condensation and cloud top cooling on the boundary layer rolls are clarified by considering simulations with and without these effects. Simulations with the cloud top entrainment instability suppressed give a stratocumulus cloud deck. There is little observational evidence to indicate any dominance of two-dimensional motions in such conditions. However the results can provide insight into the dynamics of a boundary layer with stratocumulus and highlight differences from the case with broken clouds.

Before presenting the results of this study the details of the numerical model and the solution procedure are presented. The small scale parametrization used for this study is conceptually the same as that needed in 3-D Large Eddy simulations (Deardorff 1974). The method of incorporating effects due to condensation in this parametrization is novel and discussed in detail.

Numerical Model and Turbulence Closure

a) Basic equations.

The momentum equations considered are the two-dimensional ensemble-averaged equations for an incompressible Boussinesq fluid. In Cartesian (x, y, z) co-ordinates rotating about the z-axis and with gravity parallel to the z-axis these are:

$$\frac{\partial u}{\partial t} + u\frac{\partial u}{\partial x} + w\frac{\partial u}{\partial z} = -\frac{\partial p}{\partial x} - \frac{\partial p_0}{\partial x} + fv + \frac{\partial \tau_{11}}{\partial x} + \frac{\partial \tau_{13}}{\partial z} \qquad -1.$$

$$\frac{\partial v}{\partial t} + u\frac{\partial v}{\partial x} + w\frac{\partial v}{\partial z} = -\frac{\partial p_0}{\partial y} - fu + \frac{\partial \tau_{12}}{\partial x} + \frac{\partial \tau_{23}}{\partial z} \qquad -2.$$

$$\frac{\partial w}{\partial t} + u\frac{\partial w}{\partial x} + w\frac{\partial w}{\partial z} = -\frac{\partial p}{\partial z} + B + \frac{\partial \tau_{13}}{\partial x} + \frac{\partial \tau_{33}}{\partial z} \qquad -3.$$

$$\frac{\partial u}{\partial x} + \frac{\partial w}{\partial z} = 0 \qquad -4.$$

There are no variations in the y-direction except for a background pressure gradient which together with its x-component, provides the geostrophic flow making an angle α with the x-axis. Angles of α less than 90° imply that the geostrophic wind is to the right of the y-axis. p_0 is a linearly varying background pressure so that $\partial p_0/\partial x$ and $\partial p_0/\partial y$ are constants related to the components of geostrophic wind vector. p is the perturbation pressure, f is the Coriolis parameter and τ_{ij} is a turbulent Reynolds stress tensor which is derived from the parametrization discussed below. To allow for the derivation of the buoyancy B in the presence of condensation the usual (eg. Sommeria and

Deardorff 1977) atmospheric variables must be considered. ie.

$$B = \frac{g\theta}{T}\left(1 + 0.61q - q_\ell\right) \qquad -5.$$

where T is the absolute temperature, θ the potential temperature and q and q_ℓ the mixing ratios of water vapour and liquid water. To derive the buoyancy we consider equations for the liquid water potential temperature

$$\theta_\ell = \theta - \left(\frac{\theta}{T}\right)\left(\frac{L_w}{C_p}\right) q_\ell \qquad -6.$$

and total water mixing ratio

$$q_w = q + q_\ell \qquad -7.$$

For a shallow cloud layer with no precipitation these variables are conserved and are convenient for application of finite difference methods.

The governing equations are:

$$\frac{\partial \theta_\ell}{\partial t} + u\frac{\partial \theta_\ell}{\partial x} + w\frac{\partial \theta_\ell}{\partial z} = \frac{\partial H_1}{\partial x} + \frac{\partial H_3}{\partial z} + \tau \qquad -8.$$

$$\frac{\partial q_w}{\partial t} + u\frac{\partial q_w}{\partial x} + w\frac{\partial q_w}{\partial z} = \frac{\partial Q_1}{\partial x} + \frac{\partial Q_3}{\partial z} \qquad -9.$$

where H_i and Q_i are the respective parametrized turbulent fluxes. τ is a cooling term simulating radiative cloud top cooling and is discussed below. To calculate the amount of liquid water we must introduce an expression for the saturation mixing ratio q_s. This is a

complex function of temperature T and the true pressure p_T. Dynamic pressure fluctuations have a negligible effect on q_s and to allow simple but reasonably accurate calculations of condensation, q_s is taken to be given by

$$q_s = q_{so}(1 - a(\theta - \theta_o)) \exp(-bz) \qquad -10.$$

where q_{so} is the value of q_s at the surface value of T and p_T, θ_o is the potential temperature at the surface and a and b are selected to fit the true behaviour for small changes about this value. With values of θ_ℓ and q_w the liquid water is given by

$$q_\ell = \Delta q \,/\, \left(1 + \frac{a L_w}{T C_p} q_{so} \exp(-bz)\right) \qquad -11.$$

where

$$\Delta q = q_w - q_{so}(1 - a(\theta_\ell - \theta_o)) \exp(-bz) \qquad -12.$$

and

$$q_\ell \geq 0$$

Application of this simple discontinuous condensation gave significant single grid point forcing and led to a roughness in the fields. Such behaviour has been found in 3-D large eddy simulations and previous workers (Sommeria and Deardorff 1977) have suggested that allowance should be made for the statistical variations of θ_ℓ and q_w on the subgrid scale. The details of such a statistical description are important in one-dimensional boundary layer models (Yamada and Mellor 1979) but are not believed to be

critical on the mesh scales typical of a large eddy simulation. The procedure adopted here is simple but makes allowance for a typical value of variance on the subgrid-scale. A Gaussian distribution of the quantity Δq with standard deviation

$$\sigma_s = \left(\sigma_q^2 + q_{so}^2 \, a^2 \, \sigma_\theta^2 \right)^{\frac{1}{2}} \qquad -13.$$

is considered. σ_q and σ_θ are the parametrized variances of q_w and θ_ℓ calculated diagnostically from the subgrid parametrized fluxes of q_w and θ_ℓ (see below). This simple estimate of variance neglects the $q_w \theta_\ell$ covariance but should have the correct magnitude. Following the usual approximations (Sommeria and Deardorff 1977) to a Gaussian distribution the liquid water is calculated in accord with equation 11 but with

$$\Delta q = \Delta q_0 = q_w - q_{so}\left(1 - a(\theta_\ell - \theta_o)\right) \exp(-bz) \qquad -14.$$

for $\Delta q > 1.6\,\sigma_s$,

$$\Delta q = \sigma_s \left(\Delta q_0 / \sigma_s + 1.6 \right)^2 / 6.4$$

for $-1.6\,\sigma_s < \Delta q < 1.6\,\sigma_s$,

and $\Delta q = 0$ for $\Delta q_0 < -1.6\,\sigma_s$

When this procedure was used with a local pointwise evaluation of σ_s at each time step it was found to lead to a time oscillation in the liquid water content. No entirely numerical means of eliminating this

oscillation were found and it was prevented by using a space average of σ_s over the boundary layer evaluated at each time step. This is such a gross simplification that there is little point in defending the details of the basic assumptions. The procedure was successful in allowing condensation to proceed smoothly and the use of crude assumptions are justified by the observation that changing the calculated values of σ_s by ± 50% produced only slight changes in liquid water amounts.

The only remaining term in the basic equations is the radiative cooling. The present study is intended to be fairly idealised and only longwave cooling due to liquid water is considered. The blackbody emission temperature of clouds is assumed to equal that of the ground. ie. The net upward flux at a height z

$$F = A(z, \infty)\ E(0)$$

where $E(0)$ is the difference in blackbody emission between the surface and the top of the atmosphere and $A(z,\infty)$ is the total absorptivity of liquid water betwen the level z and the top of the atmosphere. To evaluate $A(z, \infty)$ the transmission function for liquid water is taken to be $T_\ell = e^{-30 q_\ell}$ in accord with average values of transmission functions over the whole radiative spectrum (see Sommeria, 1976 for details of this approach). The cooling term r in equation 8 is the vertical divergence of this flux in each grid cell. It was calculated at each time step for each column of air.

Subgrid Parametrization

The parametrization of the small-scale eddies is an extension of the model developed in previous work (M & S) to include the influence of water vapour and condensation. The model is based upon the approach of Smagorinsky (1963) extended (Lilly 1962) to include buoyancy effects. ie.

$$\tau_{ij} = \nu\left(\frac{\partial u_i}{\partial x_j} + \frac{\partial u_j}{\partial x_i}\right) \; ; \; H_i = \nu \frac{\partial \theta_l}{\partial x_i} \; ; \; Q_i = \nu \frac{\partial q_w}{\partial x_i} \qquad -16.$$

where $$\nu = l^2 S (1 - R_i)^{1/2} \qquad -17.$$

l is a length scale,

$$S = \left[\tfrac{1}{2}\left(\frac{\partial u_i}{\partial x_j} + \frac{\partial u_j}{\partial x_i}\right)\left(\frac{\partial u_i}{\partial x_j} + \frac{\partial u_j}{\partial x_i}\right)\right]^{1/2} \qquad -18.$$

and R_i is a Richardson number defined as the ratio of buoyancy production to shear production in the equation for subgrid turbulence energy. The use of the same diffusivity for θ_l and q_w as for momentum is a deliberate simplification. In previous work (Mason 1983) it was found that, in common with 3-D large-eddy simulations, the implied sub-grid temperature variance was excessive and increases if the relative diffusion of heat over momentum is increased. The problem seems to arise from the parametrization of temperature variance in the presence of sharp localised gradients.

The length scale l has a maximum value of l_o which should, remembering the observational basis for using a 2-D model, be determined by

observations. Here a value of $\ell_o = z_i/25$, where z_i is the height of the boundary layer capping inversion, is used. This is consistent with observations (Le Mone 1973) and values used in previous (M & S) studies with the present model. The other restrictions on ℓ are intended to represent physical restrictions on the small scale motions. Near the surface ℓ is made to decrease to zero in accord with observed Monin Obukhov similarity functions. In regions of stable density stratification ℓ is limited to a value varying from ℓ_o at $R_i = 0$ to zero at a critical Richardson number of 0.33. In these regions where is limited to smaller values the value of $\ell = \ell_o$ is retained for horizontal diffusion and when

$$\nu_H = \ell_o^2 \left(2\left(\frac{\partial u}{\partial x}\right)^2 + \left(\frac{\partial v}{\partial x}\right)^2 \right)^{\frac{1}{2}} \qquad - 19.$$

is greater than ν it is used with horizontal derivatives. The details of how these features are combined and their influence on the flow is discussed in M & S.

To extend the model described by M & S to include the effect of water vapour and condensation involves a revised derivation of the Richardson number R_i. This is particularly important at the inversion or cloud top and it is important to represent it in a compact and energetically consistent manner. The staggering of the variables on the grid points can be important in this representation. Here the staggered mesh used by Williams (1969) was adopted. Pressure p is evaluated at the centre of grid volumes and u and w are defined on the side and top faces of the grid volume. v, θ_ℓ, and q_w are defined on the w points. This

— allows the definition of R_i and viscosity on w points with no vertical averaging of derivatives. As noted above R_i is defined as the ratio of the buoyancy production to shear production in the equation for sub-grid energy ie. $R_i = \overline{wB'}/\nu S^2$ where $\overline{wB'}$ is the sub-grid buoyancy flux. Previous workers (eg. Sommeria and Deardorff 1977) have derived various approximate derivations of this buoyancy flux. The approach used here is based on finite difference approximations and has fewer short-comings. In the present study it involved only a small computational effort but with more complex condensation calculations it could carry a penalty. The procedure recognises that diffusion of conservative variables between grid points separated by a distance Δz involves a fractional mixing of variables at a rate of $\nu/\Delta z^2$. It follows that if the change of the combined potential energy Δ PE of both these grid points with a fractional mixing ϵ is calculated then

$$\overline{wB'} = \frac{\nu}{\Delta z^2} \frac{\Delta PE}{\epsilon} \qquad - 20.$$

To calculate Δ PE the buoyancy of the two grid points B_N and B_{N-1} is calculated as described above. The conservative variables are then considered to mix by a small fraction ϵ ie.

$$\theta^*_{\ell,N} = \theta_{\ell,N} \cdot (1-\epsilon) + \theta_{\ell,N-1} \cdot \epsilon$$

$$\theta^*_{\ell,N-1} = \theta_{\ell,N-1} \cdot (1-\epsilon) + \theta_{\ell,N} \cdot \epsilon$$

etc and new values of buoyancy B^*_N and B^*_{N-1} are calculated. Then

$$\Delta PE = \frac{\Delta z}{2} \left((B_N - B^*_N) - (B_{N-1} - B^*_{N-1}) \right) \qquad - 21.$$

For small values of ϵ the scheme reduces to that proposed by previous

workers in both saturated and unsaturated air. It has the advantage of also taking correct account of cloud top entrainment instability. In a wholly saturated or unsaturated environment the calculation is insensitive to the value of ϵ but when only one grid point is saturated, as with cloud top instability, the results can show more dependence upon ϵ . This occurs when as a result of the finite implied mixing the state of saturation is removed. In such cases the results would be correct if ϵ was equal to the actual fractional mixing in a time-step. Such an implicit scheme would be difficult to implement. Fortunately in most cases the fractional mixing per time-step is small and the use of small value of ϵ is usually both correct and unambiguous. To allow accurate finite difference calculation in 32-bit floating point arithmetic ϵ was given the finite value of 0·025. The above procedure was used to calculate both R_i and $\overline{wB'}$. The value of ν is not required for the calculation of R_i as it occurs in both the buoyancy flux and shear production and cancels. In order to avoid significant grid point forcing in the viscosity field it was found to be important to include the statistical condensation in the $\overline{wB'}$ calculation.

To complete the description of the sub-grid parametrization we note the derivation of the values of σ_q and σ_θ used in the diagnostics and statistical calculation of condensation. ie.

$$\sigma_q^2 \equiv \left(\left(\frac{\partial q_w}{\partial z} \right)^2 + \left(\frac{\partial q_w}{\partial x} \right)^2 \right) \frac{\ell^2 \cdot 2}{D_\theta C_E}$$

and similarly for

σ_θ where D_θ is constant equal to 1·25 and C_E is the stress-energy ratio taken equal to 0·3 (see M & S).

Numerical Details and Procedure

The boundary conditions, periodicity in the horizontal direction, stress free at the top of the domain and a lower turbulent flow over a surface with roughness length z_o at the base of the domain, were applied as described in M & S. The equations were solved on a Cartesian mesh uniformly spaced in the x-direction but with variable spacing in the vertical direction. The mesh used 64 points in the horizontal direction and 80 in the vertical. At the times when statistics were obtained from the model the typical model resolution can be specified in terms of the boundary layer depth z_i (500m). The vertical resolution varied from $0{\cdot}008\ z_i$ at the surface to $0{\cdot}04\ z_i$ up to about $1{\cdot}5\ z_i$. Above $1{\cdot}5\ z_i$ the mesh slowly expands to limit at about $0{\cdot}3\ z_i$ towards the top of the domain. The top of the domain was located at $10\ z_i$ to allow ample space for gravity wave motions to be dissipated by damping located above $6\ z_i$ (see M & S). The length of the domain was chosen to be $4\ z_i$ giving a horizontal mesh spacing of $0{\cdot}0625\ z_i$. It was confirmed empirically that this resolution was sufficient to give resolution independent results. Other details and the finite difference solution procedure are described in M & S.

The initialisation of each run proceeded by starting at time $t = 0$ with $u = u_g$ and θ_ℓ and q_w equal to their values in the free atmosphere profile. The one-dimensional mixing length model implied by the sub-grid turbulence closure was then time marched until the boundary layer had grown to a height of 300 m. This one-dimensional solution was then transferred to the two-dimensional domain and perturbed. In accord with

previous studies with the two-dimensional model the angle of the domain was selected to be α = 80°, ie. rolls orientated 10° to the right of the geostrophic wind. It was confirmed that with values spaced at 5° intervals this value of α gave the most energetic motions. To obtain a compromise between statistical significance and local representation, the statistics were evaluated over a time interval corresponding to a boundary layer growth of 50 m. The variables are divided into mean and fluctuating parts but the fluctuating parts are taken relative to instantaneous horizontal means rather than space and time means. This avoids changes due to boundary layer growth and inertial variations being considered as turbulence. For convenience all variables are presented relative to axes aligned with the geostrophic wind $(u_g, 0, 0)$. The space and time means of the basic variables are denoted by $\bar{u}$, $\bar{v}$ etc. and for simplicity the mean moments based on the fluctuations are denoted by $\overline{uw}$, $\overline{w^3}$ etc.

Results

a) Cases considered.

The boundary layer profiles and parameters used in the present study are based on those observed during the period 1000 to 1300 GMT on 28th September 1981 in the KONTUR experiment (summarised in Table I). During this period distinct cloud streets were observed with a basic wind speed of about 7 ms^{-1} . On other occasions with higher wind speeds (18 ms^{-1}) less distinct cloud streets were observed. Such strong wind cases were also modelled but showed no special features; the changes from the lower wind speed case were in accord with the previous study of the influence of wind speed variations (Mason 1983) and are not shown here.

The procedures necessary to allow a detailed comparison of a boundary layer model with observations have been discussed by Sommeria (1976). In such procedures it is difficult to specify the large (synoptic) scale horizontal and vertical advection with sufficient accuracy to allow the mean profiles to be maintained as observed. Here the objective is to provide a better understanding of the dynamics and these complicating influences have been deliberately excluded. A sensible choice of the undisturbed state and boundary conditions ensures dynamical agreement with observations.

The results from a series of different cases (see Table II) are presented In each case the value of surface stress was largely determined by specifying the geostrophic wind U_g and roughness length z_o . The surface heat flux is of particular dynamical importance and to ensure both

agreement with observations and comparability between the various cases this was fixed in all cases to the value of $6{\cdot}5\ Js^{-1}\ m^{-2}$. Over the sea a specified surface temperature is a more physically realistic boundary condition but it was found difficult to specify values leading to the observed heat flux. On the other hand it was found preferable to specify a surface saturation mixing ratio $q_{s0} = 1{\cdot}1\ 10^{-2}$, independent of surface potential temperature (see equation 10) rather than a water vapour flux. This provided better control of the extent of condensation. The radiative cloud top cooling was calculated with $E(0)$ (equation 15) equal to $3{\cdot}10^{-2}\ K\,m\,s^{-1}$ In the free atmosphere the potential temperature was taken to have a fixed vertical gradient $\partial\theta_0/\partial z$ and the water vapour mixing ratio was chosen to correspond to a fixed relative humidity γ. The values of the various parameters which differ between each integration are shown in Table II.

The various cases considered help to clarify the importance of various physical processes. Cases a to f have the same basic potential temperature gradient, surface heat flux and surface roughness length. Cases a, b and c also have the same basic relative humidity (30%) and geostrophic wind. Case a is the complete simulation whilst case b has no cloud top cooling and case c has neither cloud top cooling nor condensation. The parameters correspond to preliminary observations from the field study and generate a flow with about 3/8 cloud cover. With case d the role of wind shear has been examined by setting the geostrophic wind to a small value. All of these cases have a boundary layer structure with a large (- 6K) negative jump in equivalent potential temperature θ_e

(eg Deardorff 1980a) at the inversion and the cases with condensation are thus influenced by cloud top entrainment instability. A detailed calculation of the cloud top entrainment instability criterion indicates (Deardorff 1980a, Randall 1980a) that owing to liquid water loading $\Delta\theta_e$ must be more negative than a critical value. The calculation of the subgrid buoyancy flux (equation 20) implicitly includes this effect. According to Deardorff the critical value is

$$(\Delta\theta_e)_{crit} \sim \theta \Delta q_w / \alpha_w \qquad -24.$$

where α_w depends on T and has a value near 0·5. In this case $(\Delta\theta_e)_{crit}$ is ~ -3K.

In cases e and f the basic relative humidity has been increased so as to give a positive increase of θ_e at the inversion. Otherwise cases e and f correspond to cases a and b. The supression of cloud top entrainment instability reduces the boundary layer growth and allows a boundary layer with a solid cloud cover to form. In cases d, e and f there is no observational evidence to support the domination of 2-D boundary layer rolls and the simulations can only serve to indicate changes in dynamics.

Finally in case g parameters closer to those observed in the field study are considered ie. compared with case a, a reduced basic potential temperature gradient and increased relative humidity. This also results in a boundary layer with a negative jump in θ_e (- 3K cf. $(\Delta\theta_e)_{crit}$ ~ -1·3K) at the inversion and the dynamics are very similar to those of cases a and b. This final case is examined in most detail.

b) Cases a, b, c and d.

These cases are intended to show the influence of condensation and cloud top cooling on the boundary layer rolls. Fig. 1 illustrates three realisations of the vertical velocity and liquid water fields for case a. The corresponding fields for cases b, c and d are very similar. The boundary layer eddies comprise updraughts with a typical width of $0{\cdot}5\, z_i$ and individual eddies grow and decay on time scales varying from 10^3 s to $5.\ 10^3$ s. Their spacing varies between z_i and $4\, z_i$ with clouds being associated with stronger updraughts and having a spacing of about $4\, z_i$ ie. only one cloud in the whole domain. The basic flow structure appears similar to that found by M & S in a dry inversion capped boundary layer. The key dynamical parameter determining the relative role of buoyant and shear instabilities is the ratio of the Monin-Obukhov length L ($L = u_*^3/bk$ where b is the surface buoyancy flux and k the Von Karman constant) to z_i. In case a this ratio has a value of -0·26 whilst in M & S's study it had a value of -0·3. The irregular form of the motions suggest that the large scale motions should be appreciably three-dimensional and would prevent a spectral gap from being observed at scales between the large roll wavelength and the smaller parametrized scales.

The mean boundary layer profiles for case a are shown in Fig. 2. Those for cases b and c are very similar apart from changes in the boundary layer temperature arising from varying boundary layer growth and cloud top cooling. The region of relativily warmer and dryer air occurring just above the inversion is due to energy conserving finite difference errors and has little influence on the dynamics. All of the

profiles are typical of a well mixed boundary structure. The saturation value of the water vapour mixing ratio is shown and it is evident that the mean relative humidity at the top of the boundary layer is 98% .

The mean liquid water content is shown on Fig. 3 and has a peak value of about 0·4% q_{so} . However the peak liquid water content of individual clouds is about 2% q_{so} corresponds to a liquid water mixing ratio of $2 \cdot 10^{-4}$. The mean cloud top cooling $\overline{\tau}$ is distributed over a depth of about 100m and the total cooling, $0 \cdot 5\ 10^{-2}$ k m s^{-1} , is roughly equal in magnitude to the surface heat flux. Fig. 3 also shows the heat flux profiles for the three cases. In case c there is no condensation and the heat flux profile is similar in form to that observed (eg. Caughey and Palmer 1979) in a dry convective boundary layer. The downwards heat flux at the inversion is larger than usually observed but as discussed below in connection with the entrainment rates, this difference arises from the very small heat flux and consequent importance of the water vapour flux. The downwards buoyancy flux at the inversion remains as expected in a dry convective boundary layer

With cases a and b the profiles show a large upwards heat flux due to the presence of liquid water. The rate of increase of liquid water with time is a negligible source of energy and the high correlation between liquid water and rising motion ($\overline{wq_l} / (\overline{q_l^2} . \overline{w^2})^{1/2} \sim 0.55$) arises from evaporation occurring at cloud top rather than at cloud base. The maximum concentrations of liquid water are located near the top of the strong updraughts and move steadily from right to left of the illustrations shown in Fig. 1. There is a tendency for cloud to trail behind the updraughts.

The profile of $\overline{w q_\ell}$ for case a is shown in Fig. 7 and can be used to infer the upwards heat flux associated with liquid water. This is about twice the total heat flux and it is clear that the upwards heat flux conceals a downwards flux of $\overline{w \theta_\ell}$ of about the same magnitude. The gradient of the heat flux below cloud base indicates the rate of change of the boundary layer temperature and, as a result of extra entrainment, the warming in cases a and b is roughly twice that in case c.

The total and the parametrized parts of the buoyancy flux profiles are given in Fig. 4 and show essentially the same features as the heat flux. The small scale parametrized flux provides all the transfer at the surface and a significant contribution at the inversion. Although all entrainment is ultimately due to small scale mixing the finite value of $\overline{w^2}$ at the inversion allows much of the entrained flux to appear on the resolved scale. The appearance of entrainment as a resolved scale feature suggests that resolved scale motions are crucial to the entrainment process. In fact, in case c the parametrized flux at the inversion is small and of opposite sign to the large scale flux. In previous studies with a dry boundary layer this parametrized flux had the same sign as the resolved scale flux and the opposite sign here is due to the importance of water vapour (but not condensation) in the buoyancy. In cases a and b the parametrized flux is much larger and of the same sign as the resolved flux. The main reason for the increase is the sub-grid representation of the cloud top entrainment instability. There are high eddy viscosities associated with the unstable moist air in clouds, but owing to the small gradients in clouds these are less important. In the model the cloud top entrainment instability causes both small scale mixing at the cloud top and

large scale energy release through the consequent cooling of cloud tops. The net increase in turbulence energy production is small and suggests that the entrainment proceeds with "marginal" energy release. If entrainment occurred with a large liquid water content in the boundary layer the temperature flux at the inversion would be $\sim w_e \Delta\theta_e$ (where w_e is the entrainment velocity and $\Delta\theta_e$ the jump in equivalent potential temperature). In case a $w_e \Delta\theta_e$ is $3{\cdot}9.10^{-2}$ K m s^{-1} and much bigger than the observed value of $\overline{w\theta}$ $1{\cdot}2.10^{-2}$ K m s^{-1} which occurs with fractional cloud cover.

In case b with no cloud top cooling the entrainment rate is only slightly reduced and the overall dynamics are similar to case a. The cloud top cooling in case a is too small to allow a clear identification of its effects. It occurs towards the top of the boundary layer and must thus tend to increase the potential energy of the system. The cooling is small compared with the entrainment of warm (θ_ℓ) air at the inversion and it is paradoxical that in case a, with cloud top cooling, the boundary layer warms most rapidly. Fig. 4 illustrates the vertical velocity variance profile for these cases. The increased entrainment rate in case a (see Table III) is seen to be associated with slightly more vigorous boundary rolls. The value of the total resolved scale buoyant turbulent production $w_*^3 = \int \overline{wB}\, dz$ (Table III) is also slightly greater in case a but the small size of the increase indicates that any effect due to the cooling producing a buoyancy flux is offset by increased entrainment. Overall it seems reasonable to conclude that the cooling increases entrainment and gives a modest increase in turbulent energy. The very similar values of w_* in cases b and c are a striking illustration of the marginal energy

release associated with the entrainment instability in case b.

It will become clear from the detailed study of case g below that shear production of turbulence is small away from the surface. The shear stress profile for case a is shown in Fig. 3 and the profiles for cases b and c are almost identical. They are typical of a well mixed convective boundary layer and very similar to those seen in the model results of M & S. To confirm that the wind shear had no significant effect on entrainment rates, case d with u_g reduced to 1 m s^{-1} and with the other parameters as in case c was considered. The results (Table III) confirm that the shear in cases a, b and c has little influence on entrainment.

c) Cases e and f.

These correspond to cases a and b respectively with the basic relative humidity increased to a value of 80% . This is sufficient to ensure a positive jump in θ_e at the inversion and to suppress cloud top entrainment instability. The combination of a reduced entrainment rate and a higher basic humidity gives a boundary layer with solid cloud cover and a cloud base close to ground level. In case e with cloud top cooling the mean boundary layer temperature falls steadily and entrainment continues to decrease. This integration was halted at $z_i \sim 400$m (40,000 time steps) to avoid the waste of computer time in continuing to $z_i \sim 500$m. At this time the jump in θ_l at the inversion is about 6K and provides a strong limit to boundary layer growth. The value of w_e given in Table III is an average for growth over the interval (z_i=350 to 400m) for which

statistics were acquired. Fig. 5 shows the basic boundary layer profiles for this case. All the variables show a sharp change at the inversion and the finite difference errors mentioned before are evident. The liquid water mixing ratio can be accurately estimated from the crossing of the q and q_s profiles and has a peak value of about 10^{-3}. Condensation causes an apparently stable temperature gradient in the boundary layer. The distribution of the cloud top cooling is indicated and the total cooling is $3 \cdot 10^{-2}$ K m s^{-1} (equivalent to a buoyancy flux of 10^{-3} m^2 s^{-3}). This is much greater than the surface heat flux and results in the flow being driven by downwards convection. The flow field consists of much more regular and steady eddies than those of cases a to d and the convection is dominated by rolls with a wavelength of 2 km (5 z_i since $z_i \sim 400$). The rolls were obtained in a domain of length 4Km and the downdraughts have about half the width of updraughts. Fig. 6 shows the buoyancy flux and vertical velocity variance. This shows that the buoyant turbulence energy production is dominated by cooling at the cloud top and the increase in $\overline{w^2}$ corresponds to the increase in w_6^* (Table III). The downwards nature of the convection is well illustrated by the $\overline{w^3}$ and $\overline{wq_\ell}$ profiles shown in Fig. 7 In case a the $\overline{w^3}$ profile shows the upwards flux of $\overline{w^2}$ characteristic of a convective boundary layer whilst in case e, $\overline{w^3}$ shows an entirely downwards flux. $\overline{wq_\ell}$ is also mainly negative in case e. The hydrolapse in the boundary layer is very small and fluctuations in liquid water content are mainly due to temperature fluctuations. The cool descending plumes are thus associated with a negative $\overline{wq_\ell}$. Near the inversion there is a small region of positive $\overline{wq_\ell}$ linked with the entrainment of overlying dryer air.

It is of some interest to examine the details of the re-distribution of cloud top cooling over the boundary layer. This is best considered in terms of the conserved variable θ_ℓ. The cooling produces a peak downwards flux of $\overline{w\theta_\ell}$ which is comprised of nearly equal contributions from $\overline{wq_\ell}$ and $\overline{w\theta}$. This peak has a value of 63% of the total cooling and is located at $z = 0{\cdot}68\, z_i$. The remaining 37% of the total is balanced by cooling above $z = 0{\cdot}68\, z_i$ and entrainment. The flux of $\overline{w\theta_\ell}$ due to entrainment can be calculated from the jump of θ_ℓ at the inversion (8·7K) and the entrainment velocity ($5{\cdot}10^{-4}$ m s^{-1}) and only amounts to 15% of the cloud top cooling. This confirms the view that the cooling occurs in the turbulent boundary layer and does not directly contribute to entrainment. Half the cooling is redistributed by condensation and evaporation. Condensation, rather than enhancing the production of turbulence energy has halved it.

Statistics for case f (no cloud top cooling) were obtained over the usual height range of z_i = 450 to 500m. At this time the peak liquid water content is almost exactly that seen in case e and apart from a smaller (1·5K) jump in θ_ℓ at the inversion the basic boundary layer profiles are very similar to case e. The surface humidity flux is $3{\cdot}2.10^{-6}$ m s^{-1} and is twice that occurring in case e but much less than the value, of $2{\cdot}1.10^{-5}$ m s^{-1} occurring in run a (see Table II). The total (Fig. 6) and subgrid parts of the buoyancy flux are very similar to those occurring in a dry boundary layer. The small positive buoyancy flux occurring above the inversion is due to finite difference errors and corresponds to the reduced gradient in the static stability in the region just above z_i. The $\overline{w^2}$ (Fig.6) and $\overline{w^3}$ (Fig.7) profiles are similar to

those of cases a to d and $\overline{wq_\ell}$ (Fig. 7) shows an upwards flux over most of the boundary layer. This is a large contribution to the buoyancy flux and at 0·9 z_i the $\overline{w\theta_\ell}$ (not shown) profile shows a downwards flux of similar magnitude to the surface flux. Condensation is providing a significant energy source and causing extra entrainment. The positive value of $\overline{wq_\ell}$ arises from both the upwards humidity flux and also the rate of increase of q_ℓ with time. An analogy of the process of condensation reducing the buoyancy flux due to cooling at the inversion is a similar effect that could occur with surface heating giving warm updraughts with reduced liquid water. In the present case the heating is too small compared with the upwards moisture flux to give such an effect. It is only likely to occur if in spite of surface heating the boundary layer growth rate is very small.

d) Entrainment rates.

The values of the boundary layer growth rate W in each case are given in Table III. The observed rates can be compared with calculations of encroachment ie. $w_{ec} = b/(z_i \frac{\partial B}{\partial z})$ where the surface buoyancy flux b and basic buoyancy gradient $\partial B/\partial z$ include the influence of moisture. In spite of including moisture in this way the value of the ratio w_e/w_{ec} is $\sim 1{\cdot}8$ in cases c and d and greater than the value 1·1 typical of a dry convective boundary layer. As noted above the profile of $\overline{wB}$ (Fig. 4) for case c is typical of a dry convective boundary layer and does not in itself suggest large entrainment. The buoyancy flux is the dynamically important quantity and it is reassuring that it is the same

as for a dry boundary layer The relatively large value of entrainment occurs because the temperature flux is small and the moisture flux, unlike the temperature flux, shows little decrease with height over the depth of the boundary layer. In case c about 30% of surface buoyancy flux is due to water vapour and this part of the buoyancy flux extends to the top of the boundary layer. This allows the temperature flux (Fig. 3 case c) to show the large entrainment implied by the value of w_e/w_{ec}. In correspondence with the entrainment, case c has a much larger value of jump in θ ($\Delta\theta \sim 2{\cdot}8$K) than would occur in a similar case with no moisture ($\Delta\theta \sim 0{\cdot}5$K M & S). In cases a and b the even higher value of entrainment w_e/w_{ec} 3·8 is attributable to the cloud top entrainment instability mechanism. In these cases it is evident that the rate of boundary layer growth is exactly that needed to maintain the top of the boundary layer close to saturation and to produce scattered clouds. The boundary layer growth is determined by a balance between the surface humidity flux and the entrainment of dry air at the inversion.

In case e the cloud top cooling exceeds the surface heating and no encroachment should occur. In such cases, as noted by Deardorff (1980b) the entrainment should depend on a Richardson number characterising the ratio of the boundary layer turbulence intensity to the buoyancy jump at the inversion. Owing to the cooling this Richardson number will progressively increase with time and the entrainment rate will decrease. A comparison of the value of the entrainment rate and the corresponding Richardson number $R_{i*} = z_i \Delta B / w_*^2 \approx 400$ (where ΔB is the buoyancy jump at the inversion) shows agreement with Deardorff's (1980b) empirical results for a cloud capped boundary layer.

In case f We/Wec is $\sim 2{\cdot}9$. The increase over the dry boundary layer cases is not due to any entrainment instability but is a consequence of the latent heat release in the solid cloud cover. The boundary layer mixing ratio is close to the surface value and the warming due to the liquid water content, increasing as the boundary layer grows, is $4{\cdot}7\ 10^{-3}\ K\ m^{-1}$. Including this effect in the encroachment calculation gives a revised value of $Wec = 1{\cdot}8\ 10^{-3}$ m s and We/Wec then equals ~ 1.7 in better agreement with case c and d.

e) Case g.

The parameters for this case were selected after the detailed analysis of data from the KONTUR experiment was complete and are closer to those (Table I) prevailing during the selected measurement period. The basic static stability is half that prescribed for cases a to f and the basic relative humidity is increased to 65%. The value of z_o has been reduced to obtain a value of stress closer to that observed. Cloud top cooling has not been included but would, judging by the results from case a, be a minor influence. Profiles of the basic variables are shown in Fig. 8. Owing to the reduced static stability the boundary layer eddies generate larger undulations of the inversion cap and give a more gradual appearance to the mean inversion. The jump of θ_e at the inversion is about - 3K and as noted above is sufficient to give cloud top entrainment instability. The entrainment rate is much larger than in cases a and b and $We/Wec \sim 7.2$. This rapid entrainment is needed to prevent the formation of complete cloud cover and is mainly a consequence of the increased basic relative humidity. It is sufficiently rapid to cause the significant vertical gradients evident in the u, v and q profiles. The gradient in

the q profile results in a lowering of the mean cloud base relative to that seen in cases a and b.

The buoyancy flux profile (Fig. 9) shows the same features as those discussed in cases a and b and illustrates the dynamical similarity with those cases. The water vapour flux profile is also similar to that occurring in cases a and b (Fig. 3) but owing to the more rapid growth of the boundary layer the tendency to dry the lower part of the boundary layer is more evident. The profiles of the various components of the turbulence energy have a form similar to that discussed in previous studies (M & S) and can be compared with observations from the KONTUR experiment. The observations (A.L.M. Grant, private communication) suggest that below the inversion $\overline{w^2}$ was nearly independent of height and had a value of about $0{\cdot}06\ m^2\ s^{-2}$. The model results are in fair agreement and suggest a typical value of about $0{\cdot}08\ m^2\ s^{-2}$. The observations of $\overline{u^2}$ and $\overline{v^2}$ show about 50% scatter but suggest $\overline{u^2} \sim \overline{v^2}$ and values varying from $0{\cdot}15\ m^2 s^{-2}$ at about $0{\cdot}75\, z_i$ to $0{\cdot}20\ m^2 s^{-2}$ at $0{\cdot}1\, z_i$. There are few observations in the middle of the boundary layer. The model values of $\overline{v^2}$ are in accord with the observations at $0{\cdot}75\, z_i$ but the lower values of $\overline{u^2}$ and the minimum of $\overline{v^2}$ in mid-boundary layer are not confirmed. Any departures from strict two-dimensionality would account for the isotropy of $\overline{u^2}$ and $\overline{v^2}$ and some of the extra energy in $\overline{u^2}$ and $\overline{v^2}$ is due to scales larger than those represented (2 km) in the model.

The turbulence energy balance occurring in the model rolls without condensation has been discussed in some detail by Mason (1983) and here we conclude with a brief examination of the balance for case g. Fig. 10

shows the components of the resolved scale energy budget. The total production can be compared with the $\overline{wB}$ profile (drawn on the same scale in Figure 9) to reveal the shear production. The net shear production of roll motion is close to zero and consists of a small positive contribution at the inversion with a near zero value elsewhere. The shear production dominating at the surface is almost entirely of the cross roll (roughly u-direction) component. The total transport leads to a fairly uniform profile of dissipation. This has fairly constant value in mid-boundary layer and increases both at the surface and below the inversion. Such a large increase below the inversion does not occur in cases c, d, e and f and is due to increased small scale diffusion associated with the cloud top entrainment instability The values of the components of the turbulent transport are shown in Fig. 11 and again these are similar to those found in a dry convective boundary layer. In the main boundary layer $\overline{w^3}$ leads to the main redistribution but at the top of the boundary layer $\overline{wp}$ dominates. The total flux of energy leaving the boundary layer ($\overline{wp}$ above z_i) is about 10% of the total buoyant energy production w_*^3 . This is due to the upwards radiation of gravity waves and can be compared with the heuristic model for predicting the gravity wave amplitude discussed in M & S. The heuristic model - treating boundary layer undulations as low moving hills - is in accord with the results presented here. M & S were mainly concerned with the momentum flux and did not note the energy flux. The momentum flux due to gravity waves generated by the boundary layer was found to be given by

$$A = \tfrac{1}{4}\left(F_T^{-2} - 1\right)^{\frac{1}{2}} F_T^2 \, w_T^2 \qquad \text{for} \quad F_T < 1$$

where $F_T = u_T \, k/N$, u_T is the relative velocity of the rolls to the air above the boundary layer, k is the wavenumber characterising the

spacing of the rolls, N is the Brunt Vaisala frequency $(\partial B / \partial z)^{\frac{1}{2}}$ above the boundary layer and w_r is a typical velocity scale of the boundary layer rolls. With w_r^2 equal to the maximum value of the $\overline{w^2}$ profile w_{max}^2 the values of A were found to agree with the model results. The energy flux associated with the stress A is $u_r A$ and the model thus gives a value of $\overline{wp}$,

$$\overline{wp}_r = \frac{1}{4}\left(F_r^{-2} - 1\right)^{\frac{1}{2}} F_r^2 \, w_r^2 \, u_r$$

To compare with the numerical simulation values of $\overline{wp}$ we note that $w_{max}^2 \sim 0.5 \, w_G^{*2}$ so

$$\frac{\overline{wp}_r}{w_G^{*3}} = \frac{1}{8}\left(F_r^{-2} - 1\right)^{\frac{1}{2}} F_r^2 \, \frac{u_r}{w_G^*}$$

In case g F_r is about 0·3 and u_r / w_G^* is about 3 so $\overline{wp}_r / w_G^{*3} \sim 0.1$ in accord with the results. For smaller values of z_i (350m) when F_r is 0·6 and close to optimum, $\overline{wp} / w_G^{*3}$ reaches values of 0·4 and the gravity waves must alter the gross boundary layer energy budget.

Conclusions

The two-dimensional numerical model of Mason and Sykes (1982) has been applied to an occasion when cloud streets were observed to form. The model uses a buoyancy dependent mixing-length hypothesis to parametrize small scale three-dimensional turbulence. This mixing-length hypothesis has been extended to include the influence of condensation. Richardson numbers are derived from a finite difference calculation of the rate of change of the energy due to small scale diffusion. This procedure allows the influence of statistical condensation to be included and makes no assumptions as to whether the grid points are located in wholly saturated or unsaturated air. The correct representation of the influence of condensation is important and the statistical condensation prevented unrealistic grid scale disturbances.

To apply the model the orientation of the two-dimensional domain relative to the geostrophic wind must be selected. An orientation with the roll axis at 10° to the right of the geostrophic wind is found to give maximum surface stress and turbulence energy production. At this orientation shear production of turbulence energy has a negligible influence on the roll motions. The model statistics and cloud generation are in reasonable agreement with the observations. The clouds form in the updraughts of the dominant boundary layer rolls. In common with other occasions when broken clouds are observed over the sea, there is a large decrease in the equivalent potential temperature at the top of the boundary layer, and the clouds are subject to cloud top entrainment instability. Such instability provides a large source of turbulence energy production

and provided clouds are present will promote rapid entrainment. It leads to the boundary layer growth rate being determined by a balance between the surface humidity flux and the entrainment of dry air so as to maintain the top of the boundary layer with a humidity just below a state of mean saturation. In this state of balance with partial cloudiness, entrainment is too rapid to allow a high liquid water content and the entrainment instability occurs with only marginal energy release. In spite of the rapid boundary layer growth the turbulence energy and dissipation in the boundary layer thus remain similar to those occurring in a dry boundary layer. Only at cloud top are the turbulence intensity and dissipation enhanced. As noted in earlier work (M & S) with a dry convective boundary layer, the moderate wind shear allows significant turbulence energy to be radiated upwards as internal gravity waves.

Realistic values of cloud top cooling are too small to allow more than a small influence on the boundary layer with broken clouds. The cooling results in a slight increase in turbulence energy and the entrainment rate. Suppression of the cloud top entrainment instability by increasing the value of the basic relative humidity produces dramatic changes to the nature of the influence of liquid water and the whole boundary layer. The boundary layers which result have complete cloud cover. In these cases there are few observational data to support the application of the two-dimensional model. The results nevertheless provide insight into the changes expected in convection dominated boundary layer rolls. With sufficient cloud top cooling, downwards convection dominates the dynamics. The cooling occurs in the cloud top rather than in the inversion and does not lead to any so called "direct" entrainment. There is no encroachment

due to surface heating and entrainment is slow and in accord with the Richardson number dependence suggested by Deardorff (1980b). Condensation, although crucial in allowing the radiational cloud top cooling, serves to substantially reduce the buoyancy flux and the turbulence energy production. It allows the cooling to be carried downwards from the cloud top as a latent heat flux. Without the cloud top cooling this complete cloud cover boundary layer grows more rapidly. Encroachment occurs because of both the surface heat flux and the rate of increase of liquid water with time. Apart from the energy source due to the increasing liquid water content the dynamics of the flow are very similar to those of a dry convective boundary layer.

References

Caughey, S.J., and Palmer, S.G. 1979 "Some aspects of turbulence structure through the depth of the convective boundary layer". Quart.J.R.Met.Soc. 105 811-829

Deardorff, J.W. 1974 "Three-dimensional numerical study of the height and mean structure of a heated planetary boundary layer" Boundary Layer Met. 7 81-106

Deardorff, J.W. 1980a "Cloudtop entrainment instability" J.Atmos.Sci. 37 131-147

Deardorff, J.W. 1980b "Stratocumulus-capped mixed layers derived from a three-dimensional model" J.Atmos.Sci. 38 495-527

Hoeber, H. 1982 "KONTUR: Convection and turbulence experiment field phase report" Hamburger Geophysikaliscahe Einzelschriften, Reihe B, No 1.

Le Mone, M.A. 1973 "The structure and dynamics of horizontal roll vortices in the planetary boundary layer" J.Atmos.Sci. 30 1077-1091

Lilly, D.K. 1962 "On the numerical simulation of buoyant convection" Tellus 14 148-171

Mason, P.J. 1983 "On the influence of variations in Monin-Obukhov length on horizontal roll vortices in an inversion capped planetary boundary layer" Boundary Layer Met. 27 43-68

Mason, P.J., and Sykes, R.J. 1982 "A two-dimensional numerical study of horizontal roll vortices in a inversion capped planetary boundary layer" Quart.J.R.Met.Soc. 108 801-823

Randall, D.A. 1980a "Conditional instability of the first kind upside down" J.Atmos.Sci. 37 125-131

Randall, D.A. 1980b "Entrainment into a stratocumulus layer with distributed radiative cooling" J.Atmos.Sci. 37 148-159

Reinking, R.F., Doviak, R.J. and Gilmer, R.O. 1981 "Clear-air roll vortices and turbulent motions as detected with an airborne gust probe and dual-doppler radar" J.Appl.Met. 20 678-685

Smagorinsky, J. 1963 "General circulation experiments with the primitive equations : 1. The basic experiments" Mon.Weath.Rev. 91 99-164

Sommeria, G. 1976 "Three-dimensional simulation of turbulent processes in an undisturbed trade wind boundary layer" J.Atmos.Sci. 33 216-241

Sommeria, G., and Deardorff, J.W. 1977 "Subgrid-scale condensation in models of non-precipitating clouds" J.Atmos.Sci. 34 344-355

Williams, G.P. 1969 "Numerical integration of the three-dimensional Navier-Stokes equations for incompressible flow" J.Fluid.Mech. 37 727-750

Yamada, T., and Mellor, G.L. 1979 "A numerical simulation of BOMEX data using a turbulence closure model coupled with ensemble cloud relations" Quart.J.R.Met.Soc. 105 915-944

Table I

Observed boundary layer structure 1000 to 1300 GMT 28th September 1981 in Kontur experiments. Typical values obtained by the Meteorological Research Flight C130 aircraft (A.L.M. Grant – private communication).

Geostrophic wind	7 m s^{-1}
Sea surface temperature	15.5°C
Surface $\overline{w\theta}$	6.10^{-3} m K s^{-1}
Surface $\overline{wq}$	$1.3\ 10^{-5}$ m s^{-1}
Surface $\overline{uw}$	0.042 m^2 s^{-2}
Boundary layer depth	520 m
Relative humidity above boundary layer	65%
Potential temperature gradient above boundary layer	$5\ 10^{-3}$ K m^{-1}

Table II. - Basic parameters for numerical run

Case	Condensation	U_g / ms^{-1}	Z_o/m	$\frac{\partial\theta}{\partial z} / K m^{-1}$	basic relative humidity	Cloud cooling.
a.	YES	7	10^{-3}	1.2×10^{-2}	30%	YES
b.	YES	7	10^{-3}	1.2×10^{-2}	30%	NO
c.	NO	7	10^{-3}	1.2×10^{-2}	30%	NO
d.	NO	1	10^{-3}	1.2×10^{-2}	30%	NO
e.	YES	7	10^{-3}	1.2×10^{-2}	80%	YES
f.	YES	7	10^{-3}	1.2×10^{-2}	80%	NO
g.	YES	7	2.10^{-4}	6×10^{-3}	65%	NO

Table III. - Results from numerical runs

Case	surface $\overline{wq}$ /ms^{-1}	W_e/ms^{-1}	W_{ec}/ms^{-1}	W_6^*/ms^{-1}	u_*/ms^{-1}
a.	2.1×10^{-5}	6.5×10^{-3}	1.7×10^{-3}	0.37	0.26
b.	2.0×10^{-5}	5.3×10^{-3}	1.7×10^{-3}	0.34	0.26
c.	1.5×10^{-5}	2.8×10^{-3}	1.5×10^{-3}	0.33	0.25
d.	1.5×10^{-5}	2.7×10^{-3}	1.5×10^{-3}	0.35	0.06
e.*	1.6×10^{-6}	0.5×10^{-3}	------	0.44	0.26
f.	3.2×10^{-6}	3.2×10^{-3}	1.1×10^{-3}	0.30	0.26
g.	1.6×10^{-5}	20.0×10^{-3}	2.8×10^{-3}	0.37	0.22

* N.B. Zi = 400m cf 500m for other cases.

Figure 1. Realisations of the vertical velocity field (Fig. 1a) and the corresponding liquid water field (Fig. 1b) for case a. The domain is 2 km wide and 4 km high but the fields presented only show the lowest 1 km. The contour intervals are 0.102 m s^{-1} in Fig. 1a and 2.0 10^{-5} in Fig. 1b. Dashed contours denote negative values.

Figure 2. Profiles of the basic boundary layer variables $\bar{\theta}$, $\bar{q}$, $\bar{q}_s$, $\bar{u}$ and $\bar{v}$ for case a.

Figure 3. Profiles of total $\overline{w\theta}$ (solid lines) and $\overline{wq}$ (dotted lines) for cases a, b and c, q_ℓ (solid lines) for cases a and b, with total $\overline{uw}$, $\overline{vw}$ (dashed lines) and cloud top cooling $\bar{r}$ (dashed lines) for case a.

Figure 4. Profiles of total $\overline{wB}$ and $\overline{w^2}$ for cases a, b and c. The parametrized parts of $\overline{wB}$ and $\overline{w^2}$ are shown by dashed lines.

Figure 5. Profiles of the basic boundary layer variables $\bar{\theta}$, $\bar{q}$, $\bar{q}_s$, $\bar{u}$, $\bar{v}$ and cloud top cooling r for case e.

Figure 6. Profiles of total $\overline{wB}$ (solid lines), $\overline{wq}$ (dotted lines) and $\overline{w^2}$ (solid lines) for cases e and f.

Figure 7. Profiles of resolved scale $\overline{w^3}$ and $\overline{wq_\ell}$ for cases a, e and f.

Figure 8. Profiles of the basic boundary layer variables $\bar{\theta}$, $\bar{q}$, $\bar{q}_s$, $\bar{q}_\ell$, $\bar{u}$ and $\bar{v}$ for case g.

Figure 9. Profiles of total $\overline{wB}$, $\overline{wq}$, $\overline{u^2}$, $\overline{v^2}$ and $\overline{w^2}$ for case g.

Figure 10. Balance of resolved scale turbulence energy equation for case g. Profiles of turbulent transport $T = \left(-\frac{\partial}{\partial z}\left(\overline{wp} + \frac{1}{2}\overline{w(u^2+v^2+w^2)}\right)\right)$ (dashed lines), total production $P = \left(\overline{wB} + \overline{uw}\frac{\partial \bar{u}}{\partial z} + \overline{vw}\frac{\partial \bar{v}}{\partial z}\right)$ (solid lines) and dissipation ϵ (dotted line)

Figure 11. Profiles of resolved scale $\frac{1}{2}\overline{w^3}$ (solid lines), $\frac{1}{2}\overline{w(u^2+v^2+w^2)}$ (dashed lines) and $\overline{wp}$ (dash-dot line) for case g.

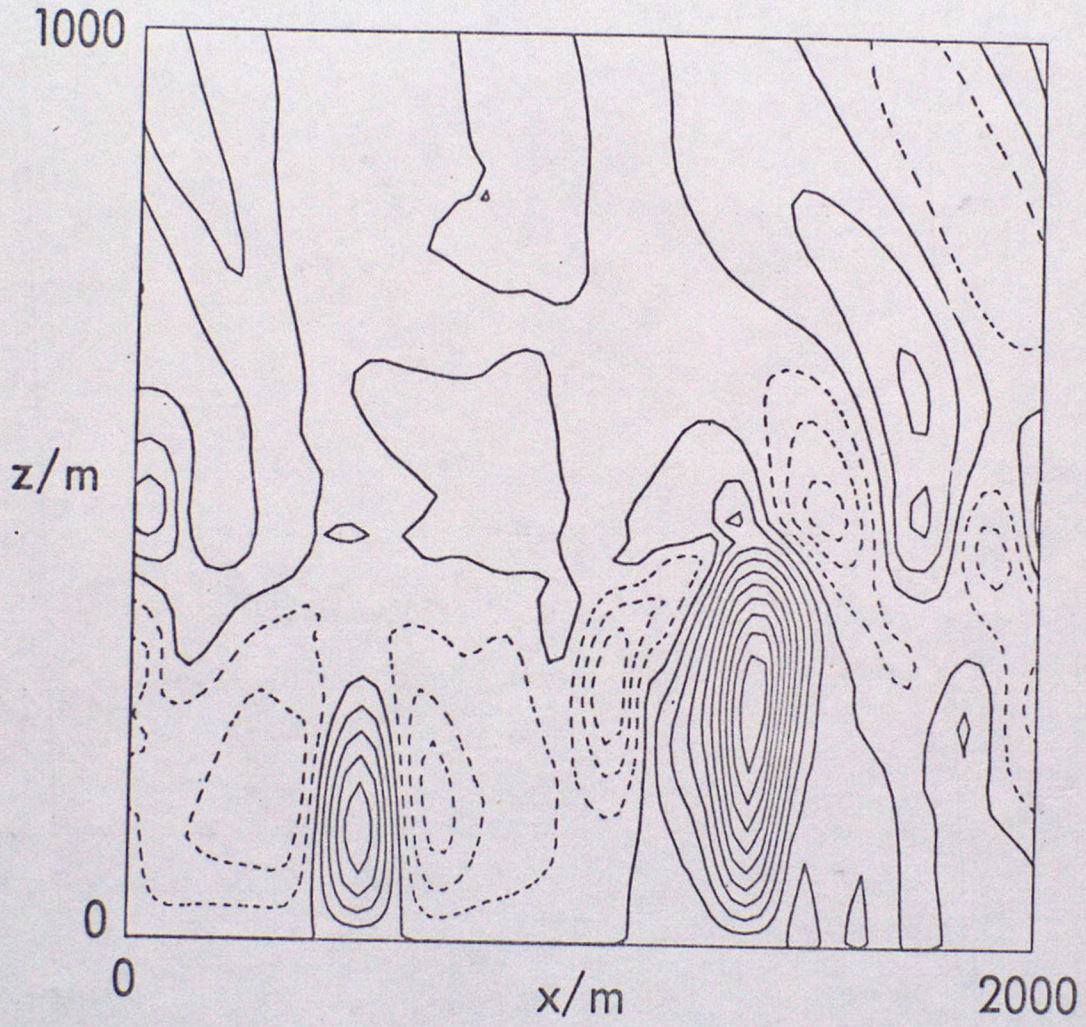

Fig 1a

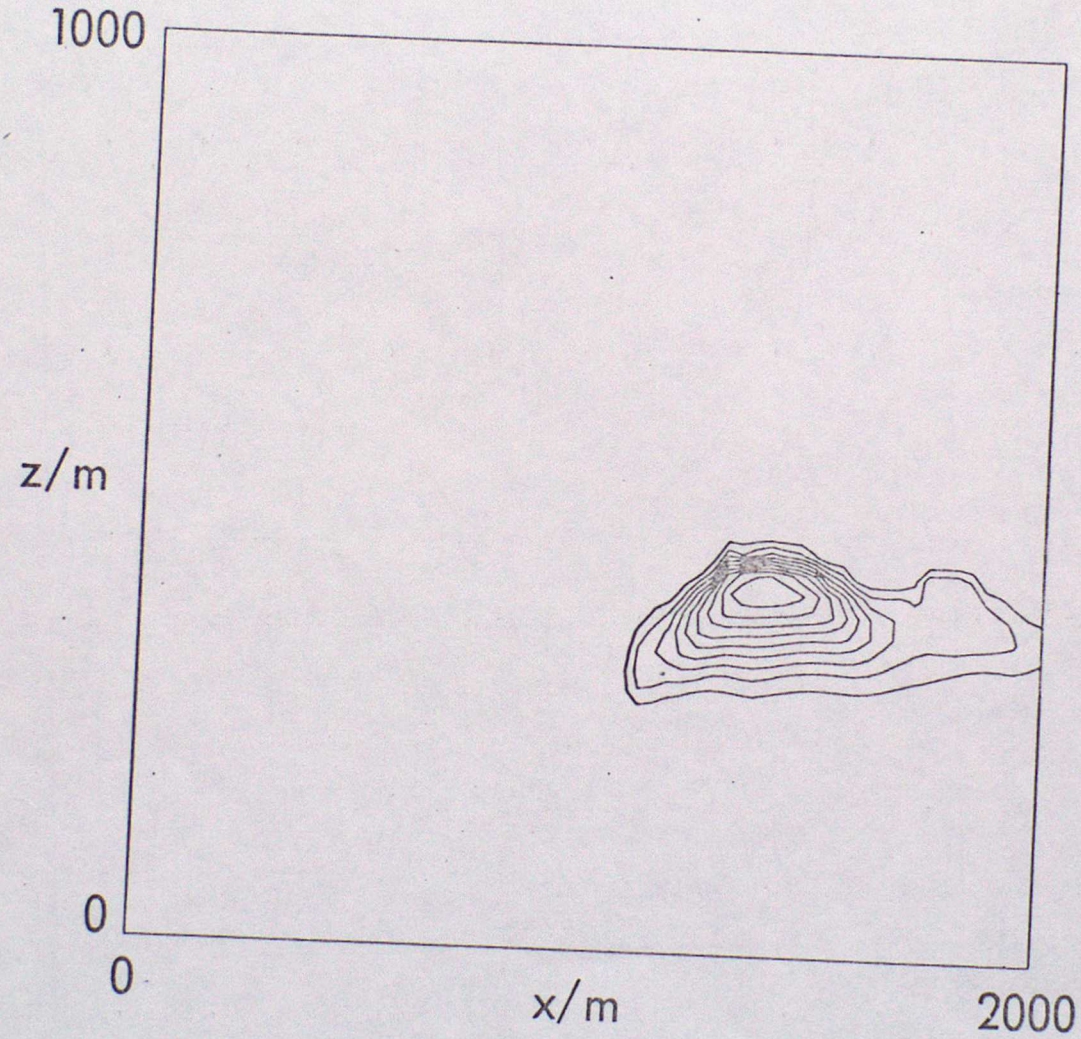

Fig 16

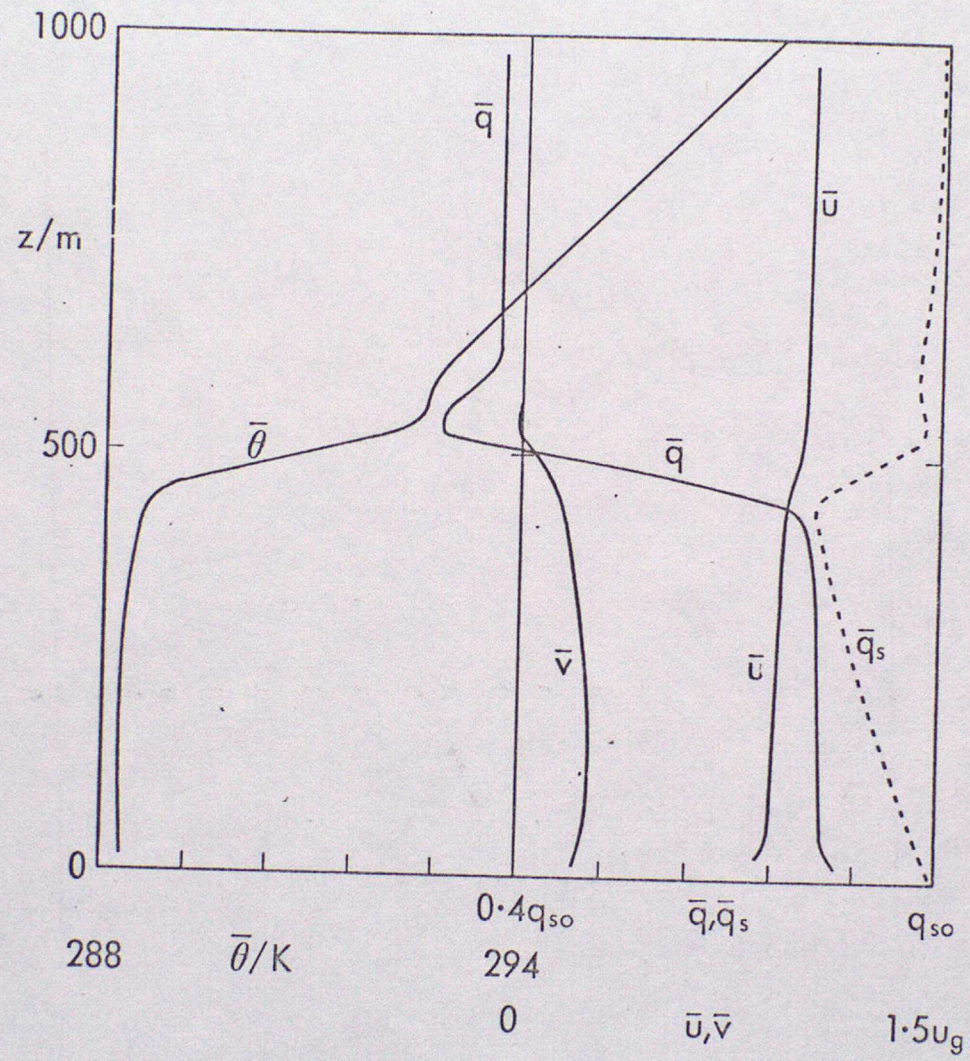
1000
z/m
500
0
$\bar{q}$
$\bar{u}$
$\bar{\theta}$
$\bar{q}$
$\bar{v}$
$\bar{u}$
$\bar{q}_s$
288
$\bar{\theta}$/K
294
0·4q_{so}
$\bar{q}$,$\bar{q}_s$
q_{so}
0
$\bar{u}$,$\bar{v}$
1·5u_g

Fig 2

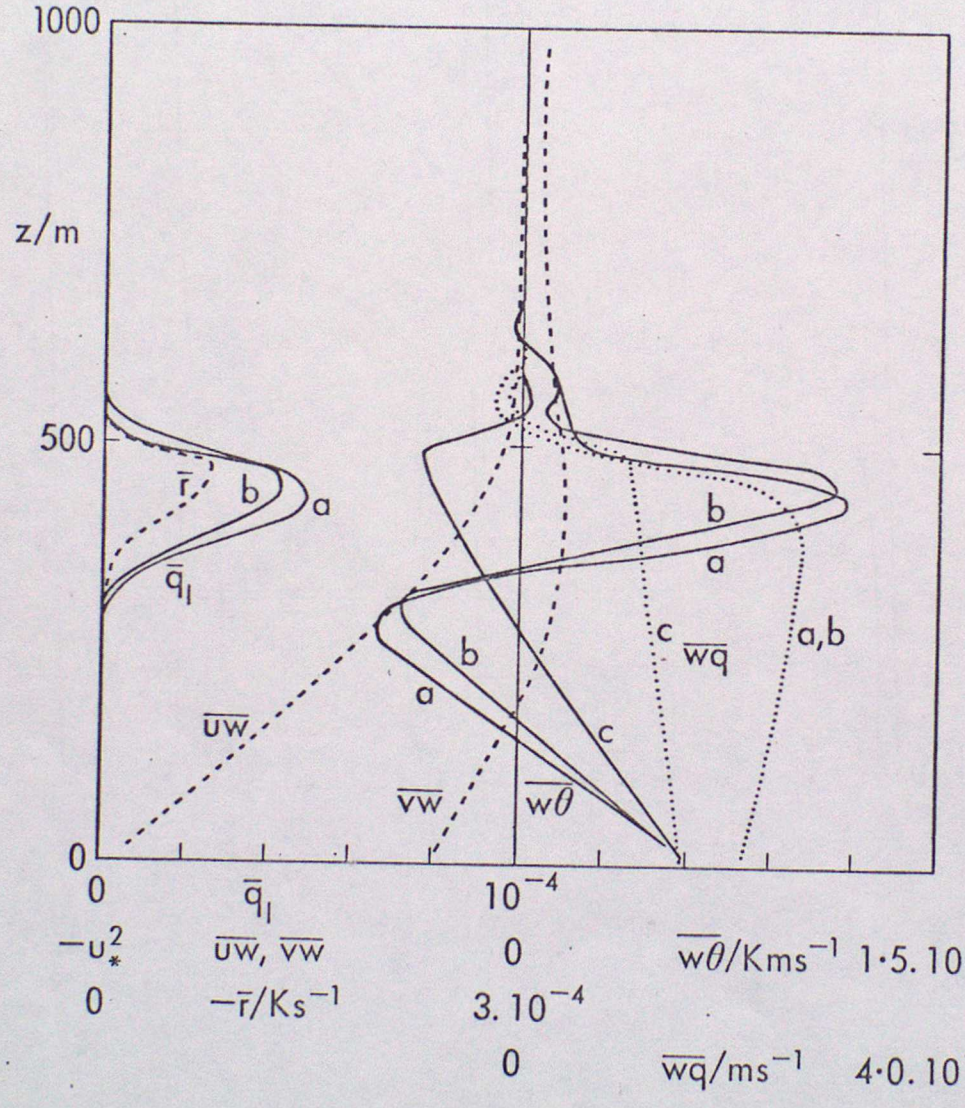
1000
z/m
500
0
$\bar{r}$
b
a
$\bar{q}_l$
b
a
c
$\overline{wq}$
a,b
b
a
$\overline{uw}$
c
$\overline{vw}$
$\overline{w\theta}$
0
$\bar{q}_l$
10^{-4}
$-u_*^2$
$\overline{uw}$, $\overline{vw}$
0
$\overline{w\theta}$/Kms^{-1}
$1{\cdot}5.10^{-2}$
0
$-\bar{r}$/Ks^{-1}
3.10^{-4}
0
$\overline{wq}$/ms^{-1}
$4{\cdot}0.10^{-5}$

Fig 3

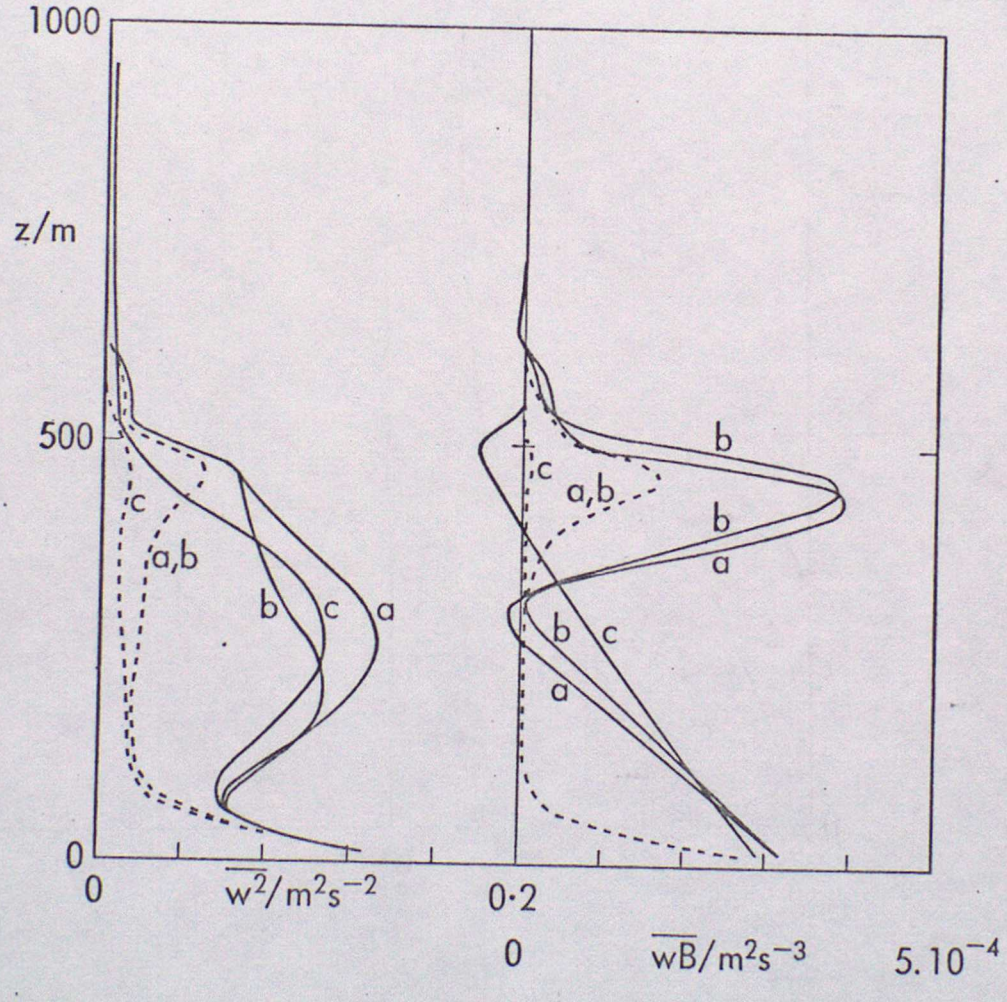
1000
z/m
500
0
0
$\overline{w^2}/m^2s^{-2}$
0·2
0
$\overline{wB}/m^2s^{-3}$
5.10^{-4}
a
b
c
a,b

Fig 4

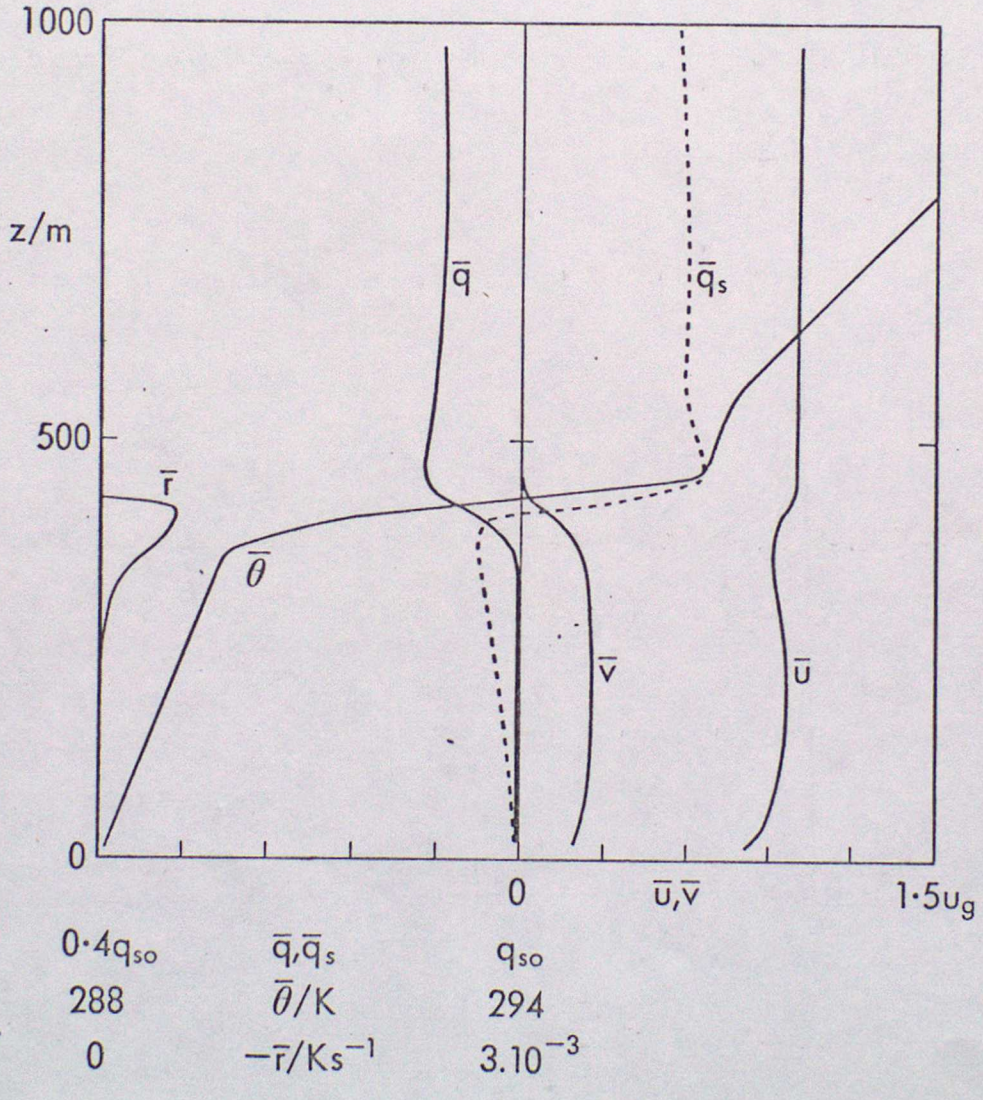
1000
z/m
500
0
$\bar{q}$
$\bar{q}_s$
$\bar{r}$
$\bar{\theta}$
$\bar{v}$
$\bar{u}$
0
$\bar{u},\bar{v}$
$1{\cdot}5u_g$
$0{\cdot}4q_{so}$
$\bar{q},\bar{q}_s$
q_{so}
288
$\bar{\theta}$/K
294
0
$-\bar{r}$/Ks^{-1}
3.10^{-3}

Fig 5

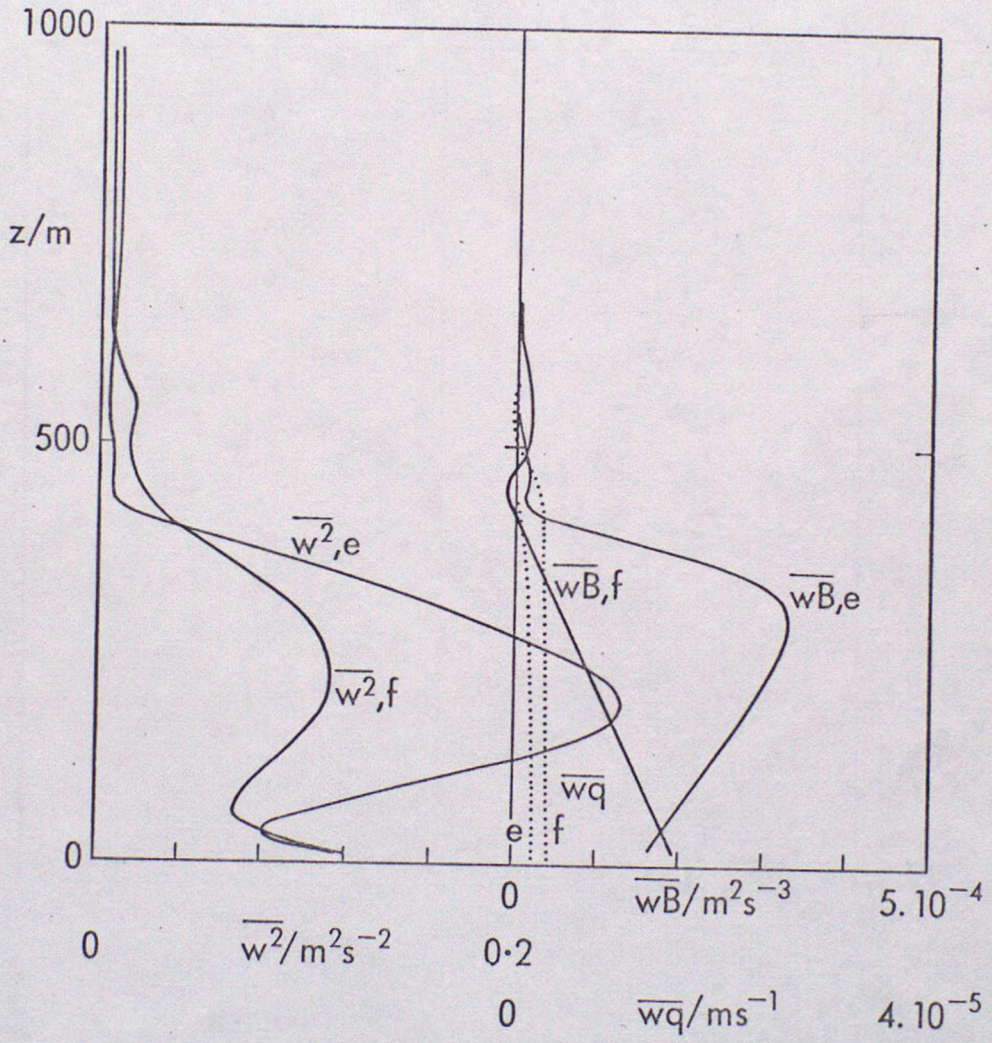
1000
z/m
500
0
$\overline{w^2}$,e
$\overline{w^2}$,f
$\overline{wB}$,f
$\overline{wB}$,e
$\overline{wq}$
e
f
0
$\overline{wB}/m^2s^{-3}$
5.10^{-4}
0
$\overline{w^2}/m^2s^{-2}$
0·2
0
$\overline{wq}/ms^{-1}$
4.10^{-5}

Fig 6

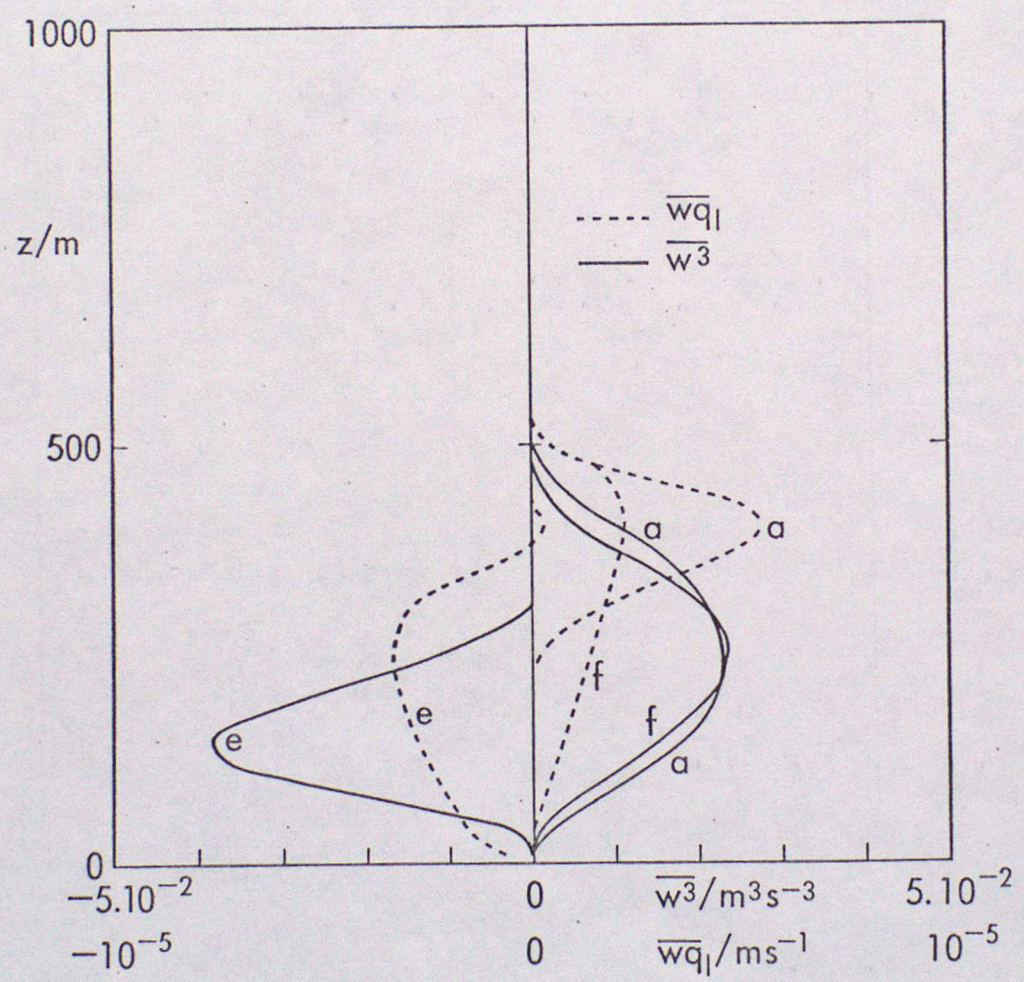
1000
z/m
500
0
$\overline{wq_l}$
$\overline{w^3}$
a
a
f
e
e
f
a
-5.10^{-2}
0
$\overline{w^3}/m^3s^{-3}$
5.10^{-2}
-10^{-5}
0
$\overline{wq_l}/ms^{-1}$
10^{-5}

Fig 7

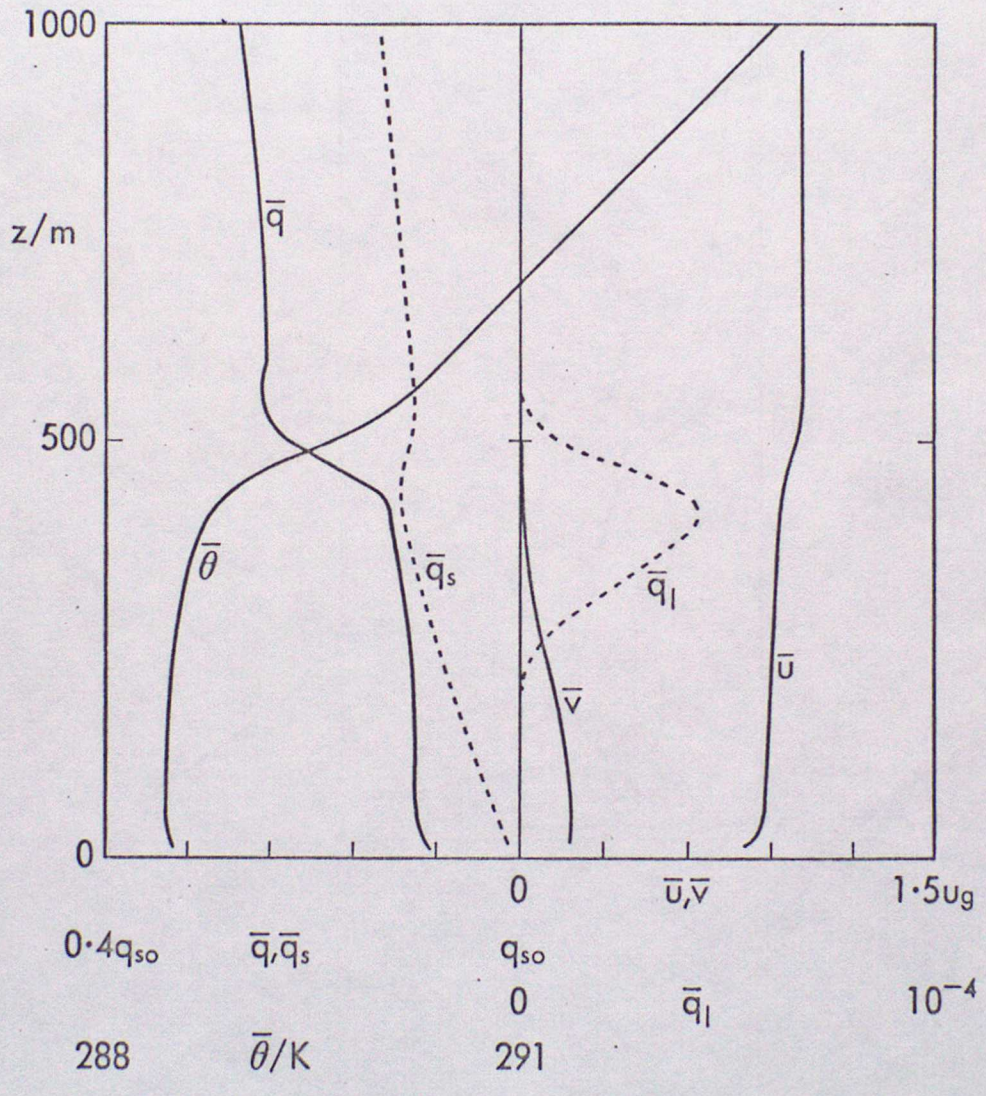
1000
z/m
500
0
$\bar{q}$
$\bar{\theta}$
$\bar{q}_s$
$\bar{q}_l$
$\bar{v}$
$\bar{u}$
0
$\bar{u},\bar{v}$
1·5ug
0·4qso
$\bar{q},\bar{q}_s$
qso
0
$\bar{q}_l$
10^{-4}
288
$\bar{\theta}$/K
291

Fig 8

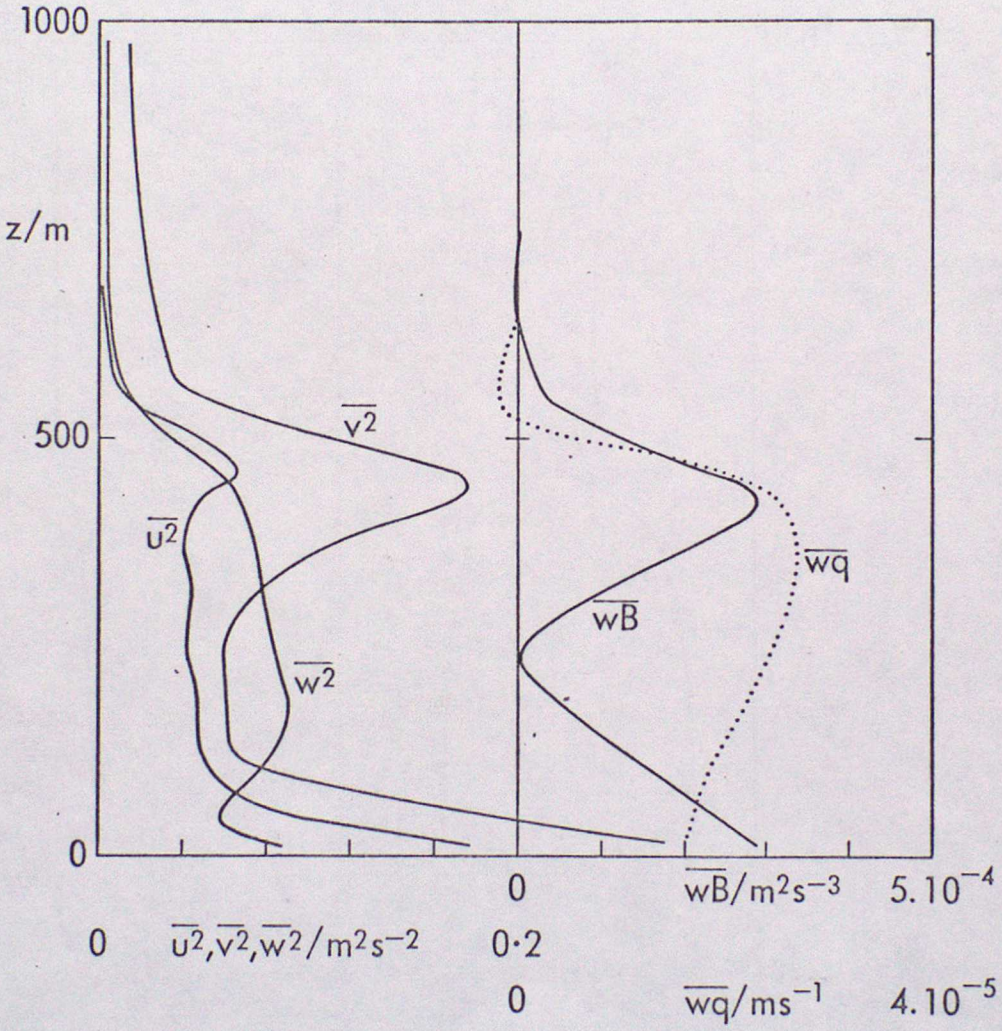
1000
z/m
500
0
$\overline{v^2}$
$\overline{u^2}$
$\overline{w^2}$
$\overline{wq}$
$\overline{wB}$
0
$\overline{wB}/m^2s^{-3}$
5.10^{-4}
0
$\overline{u^2},\overline{v^2},\overline{w^2}/m^2s^{-2}$
0·2
0
$\overline{wq}/ms^{-1}$
4.10^{-5}

Fig 9

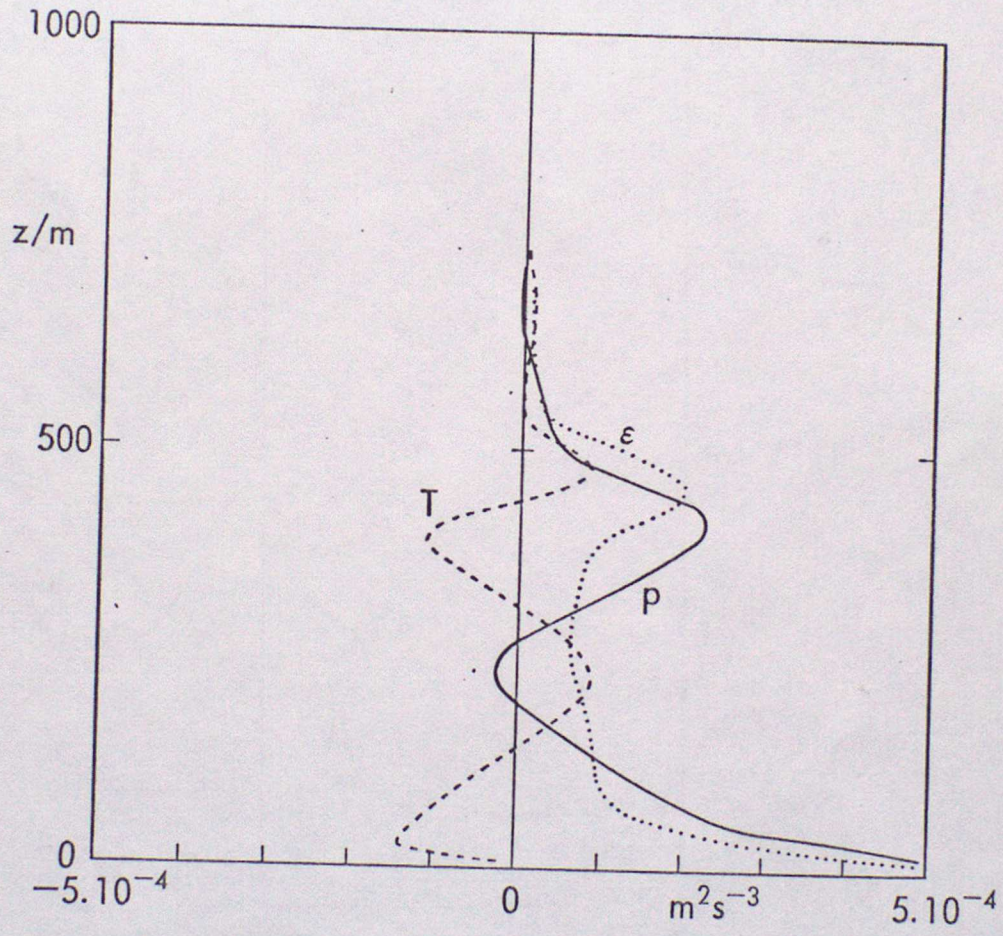

Fig 10

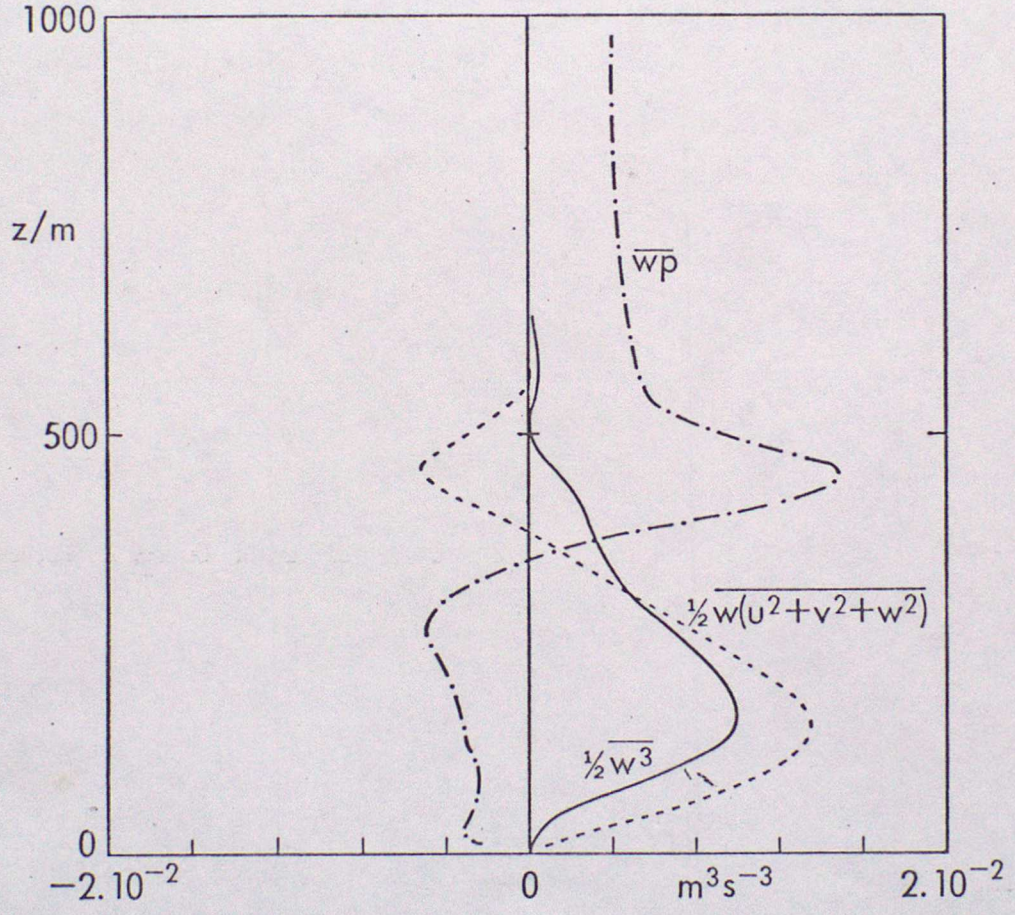
1000
z/m
500
0
$\overline{wp}$
$\frac{1}{2}\overline{w(u^2+v^2+w^2)}$
$\frac{1}{2}\overline{w^3}$
-2.10^{-2}
0
m^3s^{-3}
2.10^{-2}

Fig 11